Intermetallics 43 (2013) 24–28

Contents lists available at ScienceDirect

Intermetallics

journal homepage: www.elsevier.com/locate/intermet

Effect of strain rate on the compression behavior of TiAl and TiAl–2Mn alloys fabricated by combustion synthesis and hot press consolidation

Shili Shu, Feng Qiu, Bin Xing, Shenbao Jin, Jinguo Wang*, Qichuan Jiang*

Key Laboratory of Automobile Materials, Ministry of Education, and Department of Materials Science and Engineering, Jilin University, No. 5988 Renmin Street, Changchun 130025, People's Republic of China

ARTICLE INFO

Article history:
Received 2 March 2012
Received in revised form
23 June 2013
Accepted 8 July 2013
Available online 31 July 2013

Keywords:
A. Titanium aluminides, based on TiAl
B. Work-hardening
C. Reaction synthesis
F. Mechanical testing

ABSTRACT

Compression tests of the TiAl and TiAl–2Mn alloys have been performed in the strain rate range from 1×10^{-5} s^{-1} to 1×10^{-2} s^{-1}, and the effect of strain rate on the compression properties and work-hardening behavior of the two alloys have been investigated. Under any strain rate, the ultimate compression strength (σ^{UCS}_{true}) and the fracture strain (ε^{f}_{true}) of the TiAl–2Mn alloy are better than those of the TiAl alloy, while the work-hardening capacity (H_c) of the TiAl–2Mn alloy is lower than that of the TiAl alloy. The yield strength (σ^{y}_{true}) and H_c of the two alloys are strain rate sensitive, while the σ^{UCS}_{true} and ε^{f}_{true} are insensitive to the strain rate. With the increase in the strain rate, the σ^{y}_{true} increases, while the H_c decreases.

1. Introduction

TiAl-based alloys (γ-TiAl + α_2-Ti_3Al) have great potential as high temperature structural materials due to their low density, high melting point, good creep characteristic and excellent oxidation/corrosion resistance [1–3]. For structural components, the reliable design is of utmost importance and it requires an understanding of their mechanical properties under different loading conditions.

In the past several decades, the effect of strain rate on the deformation behavior of TiAl alloys has attracted continuous attention and was reported [4–7]. Pu et al. reported that the compression strength of TiAl–Cr–V alloy will increase at 1170 °C when the strain rate changes from 10^{-3} to 10^{0} s^{-1} [4]. Liu et al. also reported that the flow stress of the Ti–45Al–7Nb–0.4W alloy increased with the increase in strain rate (from 10^{-3} s^{-1} to 10^{-1} s^{-1}) when the tests were conducted at the temperature from 1000 °C to 1200 °C [5]. However, these works are mainly focused on the high temperature deformation behavior of TiAl alloys under various strain rates, fewer studies have probed the systematic mechanical behavior of TiAl alloys over a wide range of strain rates at room temperature. It is also important to document the mechanical response of TiAl alloys to strain rates at room temperature in order to ensure the application reliability for TiAl alloys. Moreover, work-hardening behavior is an important factor in the evaluation of the plastic deformation of materials. The deformability, ductility and toughness of materials are intimately linked to the work-hardening capacity [8]. The study on the work-hardening behavior of TiAl alloys, especially the effect of strain rate on it has never been systematic studied.

The TiAl-based alloys reported so far are mostly fabricated by casting approaches [3,9,10]. The new method of combustion synthesis and hot press consolidation takes the advantages of low energy requirement, high purity of the products, low fabrication temperature and the synthesized materials could be used directly [11,12]. Thus, the objective of this paper is to fabricate the TiAl and TiAl–2Mn alloys using the method of combustion synthesis and hot press consolidation and investigate the effect of the strain rate on the compression properties and work-hardening behavior of them at room temperature. Besides, with the purpose of trying to resolve the key problem of low ductility of TiAl alloy, the effect of Mn on the ductility of the TiAl alloy is investigated by the first principle calculation and experiment. It is expected that this study would provide a reference on the practice application and ductility improvement of TiAl alloys under various strain rate conditions.

2. Experimental

The starting materials were made from commercial powders of titanium (99.5% purity, ~25 μm), aluminum (99% purity, ~74 μm)

* Corresponding authors. Tel./fax: +86 431 85094699.
E-mail addresses: jgwang@jlu.edu.cn (J. Wang), jqc@jlu.edu.cn (Q. Jiang).

0966-9795/$ – see front matter © 2013 Elsevier Ltd. All rights reserved.
http://dx.doi.org/10.1016/j.intermet.2013.07.003

and manganese (99.5% purity, ~47 μm). Elemental powder blends corresponding to TiAl and TiAl–2Mn were mixed sufficiently by ball milling for 8 h and then cold pressed into cylindrical compacts using a stainless steel die. The powder compact with 28 mm in diameter and approximately 36 mm in height was contained in a graphite mold, which was put into the self-made vacuum thermal explosion furnace. The heating rate of the furnace was about 30 K/min and the temperature in close to the center of the compact was measured by Ni–Cr/Ni–Si thermocouples. When the temperature measured by the thermocouple suddenly rose rapidly, indicating that the sample should be ignited, the sample was quickly pressed just when it was still hot and soft. The pressure (~50 MPa) was maintained for 10 s and then was cooled down to the ambient temperature.

The phase constituents of the alloys were examined by X-ray diffraction (XRD, Model D/Max 2500PC Rigaku, Japan) with Cu Kα radiation at voltage of 40 kV using a scanning speed of 4°/min. Lattice parameter determinations were obtained using a much slower scanning speed (0.05°/min) performed around the four main peaks of TiAl from 20° to 80°. The microstructure was studied using high-resolution transmission electron microscopy (HRTEM, JEM-2100F, Japan). The cylindrical specimens with a diameter of 3 mm and a height of 6 mm were used for compression tests, and the loading surface was polished to parallel to the other surface. The uniaxial compression tests were carried out under a servo-hydraulic materials testing system (MTS, MTS 810, USA) with constant strain rates of 1×10^{-5} s^{-1}, 1×10^{-4} s^{-1}, 1×10^{-3} s^{-1} and 1×10^{-2} s^{-1}.

The calculation work was performed with the Cambridge Sequential Total Energy Package code (CASTEP) [13]. Brillouin zone was set within $3 \times 3 \times 3$ k point mesh generated by the Monkhorst–Pack scheme [14]. The plane-wave basis cutoff was set as 400 eV for all cases. We have performed more precise testing calculations with a plane-wave cutoff energy of 450 eV, however, the results changed negligibly. Therefore, the value of 400 eV for plane-wave cutoff energy is precise enough for our investigation [15]. According to our previous study and other researchers' work [16–18], the Mn atom prefers the Al site. Thus, in this work, the calculation was performed on the $Ti_{16}Al_{16}$ and $Ti_{16}Al_{15}Mn$ 32-atom supercells.

3. Results and discussion

3.1. Phase identification and microstructure

Fig. 1 shows the XRD patterns for the fabricated TiAl and TiAl–2Mn alloys. The products in the two alloys are mainly γ-TiAl and α_2-Ti_3Al phases. The volume fraction of α_2-Ti_3Al phase in the TiAl and TiAl–2Mn alloys calculated by the method of adiabatic method according to the XRD results are about 16.9 vol.% and 17.6 vol.%, respectively. The Mn element has little effect on the phase composition of the TiAl alloy. As indicated in the insert in Fig. 1, the peak position of the TiAl (111) plane shifts to higher 2θ values with the addition of the Mn element, implying a decrease in the lattice constant of the TiAl. As Mn (0.179 nm) has smaller atomic radius than Al (0.182 nm), the Mn substitution of Al results in the lattice shrink. The SEM image of the TiAl alloy fabricated by the method of combustion synthesis and hot press consolidation has been reported in our previous work [19], and the SEM image of the TiAl–2Mn alloy is similar to that of the TiAl alloy. The TiAl and TiAl–2Mn alloys have similar grain sizes of ~60 μm. The actual concentration of Mn in the TiAl–2Mn alloy detected by energy-dispersive spectra is about 1.36 at.%. According to these results, we believe that the Mn element existed in the TiAl–2Mn alloy is mainly in the form of solid solution.

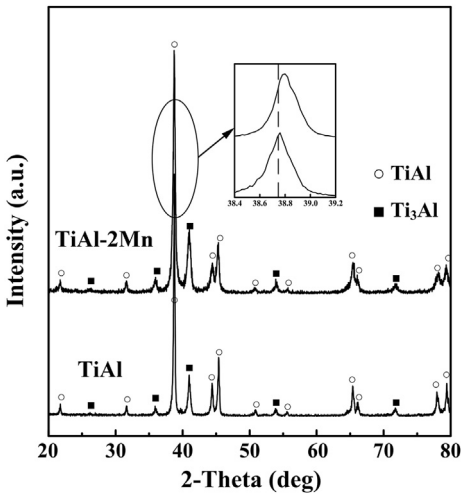

Fig. 1. XRD patterns of the TiAl and TiAl–2Mn alloys.

Fig. 2(a) and (b) shows the TEM images of the TiAl and TiAl–2Mn alloys. It can be seen from Fig. 2(a) that there are a lot of dislocations existed in the TiAl alloy. It indicates that the TiAl alloy fabricated by the method of the combustion synthesis and hot press consolidation possesses higher dislocation density. Fig. 2(b) shows a well developed subgrain structure and a kind of nanometer phase in the TiAl–2Mn alloy. The selected-area electron diffraction (SAED) pattern inserted in Fig. 2(b) obtained from area A corresponds to the $[1\bar{9}6]$ zone axis of the $Al_{19}Mn_4$. According to the HRTEM image of the $Al_{19}Mn_4$ phase, as shown in Fig. 2(c), the synthesized $Al_{19}Mn_4$ phase by the combustion synthesis reaction is in the shape of ellipse and the size is about 15 nm. Fig. 2(d) is the inverse Fourier transformation of the HRTEM image of the area B. The dislocations in TiAl are marked as the "T" shaped symbol. A large number of dislocations exist around the $Al_{19}Mn_4$ phase. It indicates the $Al_{19}Mn_4$ phase would hinder the movement of the dislocations during the following deformation. The dislocation densities in the TiAl and TiAl–2Mn alloys calculated from XRD peak profile analysis [20] are 4.24×10^{12} m^{-2} and 6.52×10^{12} m^{-2}, respectively.

3.2. Compression properties

Fig. 3 shows the compression true stress–strain curves of the TiAl and TiAl–2Mn alloys under different strain rates. The compression properties of the alloys under different strain rates are summarized in Table 1. The σ^{y}_{true} of the two alloys increases with the increase in the strain rate, while there is no significant difference in the σ^{UCS}_{true} and ε^{f}_{true} of the both alloys with the variation in strain rates. Comparing the compression properties of the TiAl and TiAl–2Mn alloys as shown in the insert in Fig. 3, it is observed that TiAl–2Mn alloy shows higher strength and better ductility than the TiAl alloy at any strain rate. At the strain rate of 1×10^{-5} s^{-1}, the σ^{UCS}_{true} of the TiAl–2Mn alloy is 125 MPa higher than that of the TiAl alloy, and the ε^{f}_{true} of the TiAl–2Mn alloy is 18.8% comparing to 17.0% for the TiAl alloy. Because the two alloys have the similar starting microstructures, like grain size and α_2 phase volume fraction, the differences in the compression properties of them could be mainly due to the exist of the nano $Al_{19}Mn_4$ phase, the well developed subgrain structure, the solid solution of Mn and the different contents of dislocation density. The higher strength of the TiAl–2Mn alloy could be mainly due to the hindrance to the slip of dislocations by the nano $Al_{19}Mn_4$ phase, the subgrain boundaries and the stress

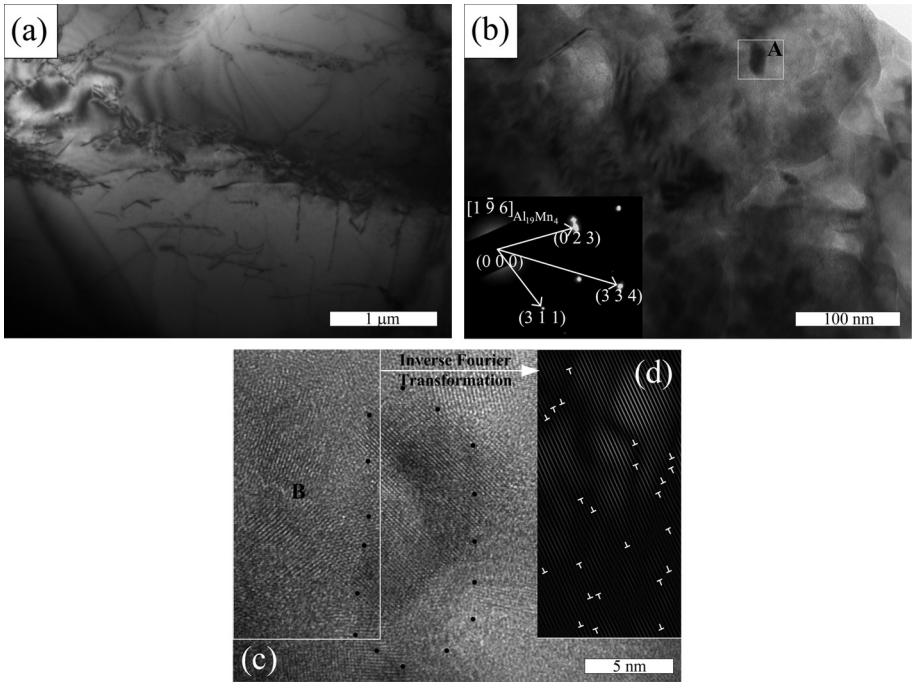

Fig. 2. TEM images of the (a) TiAl and (b) TiAl–2Mn alloys, insert: SAED pattern at the area A, (c) HRTEM image of the area A and (d) the inverse Fourier transformation of the HRTEM image of the area B.

field caused by the Mn solid solution. The ductility improvement of the TiAl–2Mn alloy is associated with the change of crystal structure by the addition of Mn element. Thus, we have investigated it by the method of first principle calculation in the following section.

3.3. Lattice parameter and elastic properties

TiAl is an intermetallic compound with an ordered $L1_0$-type crystal structure ($c/a = 1.02$). The lattice tetragonality of TiAl has been proposed to be one of the basic characteristics that relates with the intrinsic brittleness [18,21]. The lattice parameters of TiAl with and without Mn addition were calculated both by the first-principles calculation and XRD experiment, and shown in Table 2. It can be seen from the results that the Mn addition has little effect on the *a*-axes of TiAl while it strongly reduces the lattice parameter of *c*-axes. The contraction of the *c*-axes reduces the *c*/*a* ratio of the crystal lattice and therefore reduces the lattice tetragonality of TiAl. The reduced lattice tetragonality would be responsible to the ductility improvement of the TiAl–2Mn alloy because new operating glide systems could be activated [18,21]. The bulk modulus (B) and shear modulus (G) of the $Ti_{16}Al_{16}$ and $Ti_{16}Al_{15}Mn$ supercells were also calculated by the first principle calculation. According to Pugh's study [22], the quotient of B/G reflects the extent of ductility for metals and intermetallic compounds; that is, a high value of B/G means better ductility, while a low value indicates a tendency for brittleness. Table 3 shows the values of B, G and B/G of the $Ti_{16}Al_{16}$ and $Ti_{16}Al_{15}Mn$ supercells. It is noted that Mn addition improves the value of B/G, which is increased from 1.49 for $Ti_{16}Al_{16}$ to 1.98 for $Ti_{16}Al_{15}Mn$. Thus, the better ductility of the TiAl–2Mn alloy is possibly due the reduction of the lattice tetragonality and the change of the elastic properties.

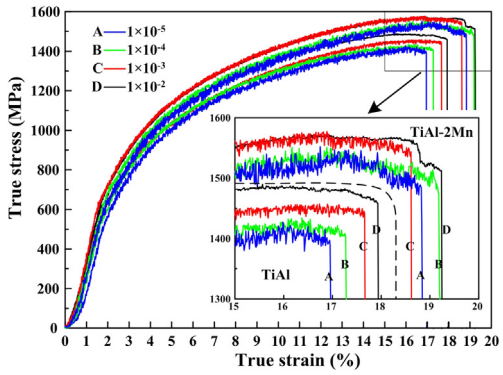

Fig. 3. Compression true stress–strain curves of the TiAl and TiAl–2Mn alloys. Insert: the magnification of the large strain region.

3.4. Strain rate sensitivity and work-hardening behavior

The strain rate sensitivity $m = \partial \ln\sigma / \partial \ln\dot{\varepsilon}$ [23] and the apparent activation volume $V^* = \sqrt{3}kT\partial \ln\dot{\varepsilon}/\partial\sigma$ [24] of the TiAl and TiAl–2Mn alloys were determined, respectively, by the isostrain method, where σ is the flow stress, $\dot{\varepsilon}$ is the strain rate, k is Boltzmann's constant and T is the absolute temperature. Strain rate sensitivity is one of the key engineering parameters to accurately predict the deformation behavior of the materials during loading [25], and the activation volume is widely used to determine the possible

Table 1
Room-temperature compression properties and work-hardening capacity of the TiAl and TiAl–2Mn alloys under various strain rates.

Sample	Strain rate (s^{-1})	σ^{y}_{true} (Mpa)	σ^{UCS}_{true} (Mpa)	ε^{f}_{true} (%)	H_c
TiAl	1×10^{-5}	403	1427	*17.0*	2.54
	1×10^{-4}	424	1434	*17.3*	2.38
	1×10^{-3}	455	1457	*17.6*	2.20
	1×10^{-2}	509	1489	*17.9*	1.93
TiAl–2Mn	1×10^{-5}	520	1552	*18.8*	1.98
	1×10^{-4}	561	1551	*19.2*	1.76
	1×10^{-3}	578	1577	*18.6*	1.73
	1×10^{-2}	597	1572	*19.3*	1.63

Table 2
The lattice parameters of the $Ti_{16}Al_{16}$ and $Ti_{16}Al_{15}Mn$ supercells and the TiAl and TiAl–2Mn alloys calculated by the first principle calculation and XRD experiment, respectively.

Method	Sample	a (Å)	c (Å)	c/a
First-principles	$Ti_{16}Al_{16}$	4.006	4.052	1.011
	$Ti_{16}Al_{15}Mn$	4.005	4.011	1.001
XRD	TiAl	3.995	4.072	1.019
	TiAl–2Mn	3.993	4.046	1.013

Table 3
Calculated bulk modulus B, shear modulus G and B/G values for the $Ti_{16}Al_{16}$ and $Ti_{16}Al_{15}Mn$ supercells.

Sample	B (GPa)	G (GPa)	B/G
$Ti_{16}Al_{16}$	111.0	74.7	1.49
$Ti_{16}Al_{15}Mn$	114.5	57.8	1.98

deformation mechanisms of materials [24,26,27]. The steady-state flow stress of the TiAl and TiAl–2Mn alloys at 0.2%, 1.0% and 2.0% plastic strain were plotted in logarithmic form as a function of the logarithmic form of the strain rate in Fig. 4(a) and (b), and the strain rate sensitivities of them are calculated from the slopes. According to the results, the m values of the two alloys are almost the same and decrease with the increase in the plastic strain. The insets in Fig. 4(a) and (b) are the plot of $\ln\dot{\varepsilon}$ vs. σ transformed from Fig. 4(a) and (b) wherein the experimental activation volumes (V^*) calculated from the slopes are indicated. The average activation volumes ($\overline{V^*}$) of the TiAl and TiAl–2Mn alloys are $22.5b^3$ and $24.6b^3$, respectively, where $b = 0.283$ nm is the Burgers vector [28]. According to the literatures [29,30], such a low-activation volume is often associated with deformation mechanism of dislocation glide process.

It can be seen from the true stress–strain curves of the samples shown in Fig. 3 that these curves all show a clear work-hardening. The work-hardening capacity of the alloys is calculated according to the formulary (H_c) ($H_c = (\sigma^{UCS}_{ture} - \sigma^{y}_{true})/\sigma^{y}_{true}$) [31] and listed in Table 1. The H_c of both the alloys decreases with the increase in the strain rate and the TiAl alloy possesses the higher H_c at all strain rates. In order to evaluate and compare the effect of the strain rate on the work-hardening behavior of the TiAl and TiAl–2Mn alloys, the normalized work-hardening rate (Θ') of the alloys tested under the strain rate of 1×10^{-5} s^{-1} and 1×10^{-4} s^{-1} was calculated. The Θ' was defined as $\Theta' = (d\sigma_{true}/d\varepsilon_{true})/\sigma_{true}$ [8,32]. The result,

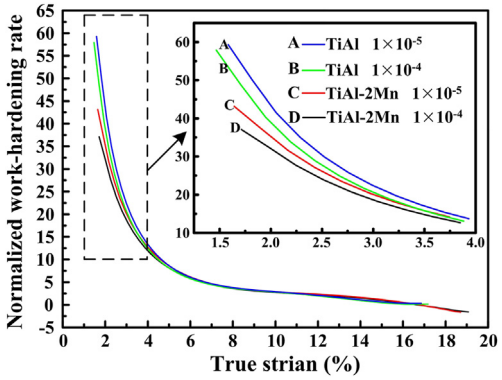

Fig. 5. Normalized work-hardening rate (Θ') vs. true strain for the TiAl and TiAl–2Mn alloys, inset: the magnification of the low strain region.

plotted as a function of the true strain in the plastic region, is shown in Fig. 5. The Θ' of the two alloys tested under both strain rates decreases with the increase in the true strain. At high strain levels (>5%), the Θ'-true strain curves are almost overlapped. It indicates that, at the last stage of deformation, the work-hardening behavior of the two alloys tested under any strain rate is similar. While it can be seen from the inset in Fig. 5 that, at low strain levels, the Θ' is affect both by the Mn addition and the strain rate. Compared to the TiAl–2Mn alloy, the TiAl alloy possesses the higher Θ', and the Θ' decreases with the increase in the strain rate. According to the results of the activation volume calculation, the deformation mechanism of both the alloys is dislocation mobility mechanism. The higher Θ' represents the more extensive interaction of the dislocations. As shown in Fig. 2, the fabricated alloys both possess a large number of dislocations. However, due to the obstruction of the nano $Al_{19}Mn_4$ phase, the start-up of the dislocations in TiAl–2Mn alloy becomes difficult. Thus, at the first stage of deformation, the dislocation interaction in the TiAl–2Mn alloy is weakened, leading to the low Θ' and H_c. The σ^{y}_{true} is the dislocation-nucleation threshold stress. With the increase of the strain rate, the σ^{y}_{true} of both alloys increases, that is, the activation of the dislocations becomes difficult with the increase in the strain rate. Consequently, the dislocation interactions at the first stage of deformation would become weak with the increase in the strain rate, which is consistent with the lower Θ' as shown in the insert in Fig. 5. Thus, the H_c of the two alloys decreases with the increase in the strain rate.

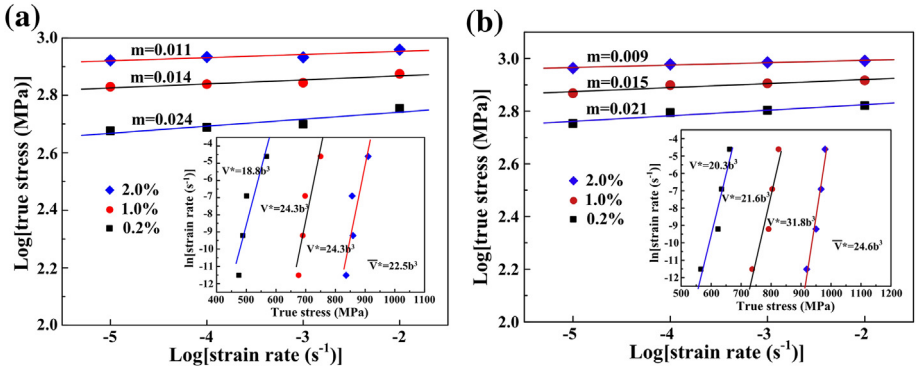

Fig. 4. Log (true stress) vs. log (strain rate) at 0.2%, 1.0% and 2.0% plastic strain for the (a) TiAl and (b) TiAl–2Mn alloys. Strain rate sensitivity is calculated from the slopes. The inserts in them are ln (strain rate) vs. true stress curves where the activation volumes are calculated.

4. Conclusions

The σ^{y}_{true} and H_c of the both alloys exhibit a remarkable strain-rate-dependent. With the increase in the strain rate, the σ^{y}_{true} of the two alloys increases, while the H_c decreases. Under any strain rate, the TiAl–2Mn alloy possesses higher strength and better ductility. The strength improvement is mainly due to the solid solution strengthening of the Mn addition, the second phase strengthening of the nano $Al_{19}Mn_4$ phase and the well developed subgrain structure. The work-hardening behavior of the two alloys could be divided into two stages. In the first stage of deformation the work-hardening behavior is affected by the Mn addition and the strain rate. While in the last stage of deformation, the work-hardening behavior of both alloys at various strain rates is similar. The TiAl alloy possesses the higher H_c at any strain rate.

Acknowledgment

This work is supported by the National Natural Science Foundation of China (No. 51171071), National Basic Research Program of China (973 Program, No. 2012CB619600), NNSFC (No. 50971065 and No. 50531030) and the Fund of Basic Scientific Research of Jilin University (No. 200903013) and the Research Fund for the Doctoral Program of Higher Education of China (No. 20100061120063) and Graduate Innovation Fund of Jilin University (No. 20121087) as well as by The Project 985-High Performance Materials of Jilin University.

References

[1] Huang SC, Hall EL. The effects of Cr additions to binary TiAl-base alloys. Metall Mater Trans A 1991;29:2619–27.
[2] Kabir MR, Chernova L, Bartsch M. Numerical investigation of room-temperature deformation behavior of a duplex type γTiAl alloy using a multi-scale modeling approach. Acta Mater 2010;58:5834–47.
[3] Appel F, Wagner R. Microstructure and deformation of two-phase γ-titanium aluminides. Mater Sci Eng R 1998;22:187–268.
[4] Pu ZJ, Wu KH, Shi J, Zou D. Development of constitutive relationships for the hot deformation of boron microalloying TiAl–Cr–V alloys. Mater Sci Eng A 1995;192/193:780–7.
[5] Liu B, Liu Y, Zhang W, Huang JS. Hot deformation behavior of TiAl alloys prepared by blended elemental powders. Intermetallics 2011;19:154–9.
[6] Luo J, Li MQ, Yu WX, Li H. The variation of strain rate sensitivity exponent and strain hardening exponent in isothermal compression of Ti–6Al–4V alloy. Mater Des 2010;31:741–8.
[7] Vaidya RU, Jin Z, Cady C, Gray GT, Butt DP. A comparative study of the strain rate and temperature dependent compression behavior of Ti–46.5Al–3Nb–2Cr–0.2W and Ti–25Al–10Nb–3V–1Mo intermetallic alloy. Scripta Mater 1999;41:569–74.
[8] Chen XH, Lu L. Work hardening of ultrafine-grained copper with nanoscale twins. Scripta Mater 2007;57:133–6.
[9] Kawabata T, Fukai H, Izumi O. Effect of ternary additions on mechanical properties of TiAl. Acta Mater 1998;46:2185–94.
[10] Su YQ, Liu C, Li XZ, Guo JJ, Li BS, Jia J, et al. Microstructure selection during the directionally peritectic solidification of Ti–Al binary system. Intermetallics 2005;13:267–74.
[11] Gotman I, Koczak MJ, Shtessel E. Fabrication of Al matrix in situ composites via self-propagating synthesis. Mater Sci Eng A 1994;187:189–99.
[12] Choi Y, Rhee SW. Effect of aluminium addition on the combustion reaction of titanium and carbon to form TiC. J Mater Sci 1993;28:6669–75.
[13] Segall MD, Lindan PJD, Probert MJ, Pickard CJ, Hasnip PJ, Clark SJ, et al. First-principles simulation: ideas, illustrations and the CASTEP code. J Phys Condens Matter 2002;14:2717–44.
[14] Pack JD, Monkhorst HJ. Special points for Brillouin-zone integrations—a reply. Phys Rev B 1977;16:1748–9.
[15] Wang HY, Si WP, Li SL, Zhang N, Jiang QC. First-principles study of the structural and elastic properties of Ti_5Si_3 with substitutions Zr, V, Nb, and Cr. J Mater Res 2010;25:2317–24.
[16] Shu SL, Qiu F, Xing B, Jin SB, Wang YW, Jiang QC. Study of effect of Mn addition on the mechanical properties of Ti_2AlC/TiAl composites through first principles study and experimental investigation. Intermetallics 2012;28:65–70.
[17] Hao YL, Yang R, Cui YY, Li D. The effect of Ti/Al ratio on the site occupancies of alloying elements in γ-TiAl. Intermetallics 2000;8:633–6.
[18] Zhou LG, Dong L, He LL, Zhang CB. Ab initio pseudopotential calculations on the effect of Mn doped on lattice parameters of $L1_0$ TiAl. Intermetallics 2000;8:637–41.
[19] Shu SL, Xing B, Qiu F, Jin SB, Jiang QC. Comparative study of the compression properties of TiAl matrix composites reinforced with nano-TiB_2 and nano-Ti_5Si_3 particles. Mater Sci Eng A 2013;560:596–600.
[20] Shan FL, Gao ZM, Wang YM. Microhardness evaluation of Cu–Ni multilayered films by X-ray diffraction line profile analysis. Thin Solid Films 1998;324:162–4.
[21] Chubb SR, Papaconstantopoulos DA, Klein BM. First-principles study of $L1_0$ Ti-Al and V-Al alloys. Phys Rev B 1988;38:12120–4.
[22] Pugh SF. Relations between the elastic moduli and the plastic properties of polycrystalline pure metals. Philos Mag 1954;45:823–43.
[23] Lian JS, Gu CD, Jiang Q, Jiang ZH. Strain rate sensitivity of face-centered-cubic nanocrystalline materials based on dislocation deformation. J Appl Phys 2006;99:076103.
[24] Asaro RJ, Suresh S. Mechanistic models for the activation volume and rate sensitivity in metals with nanocrystalline grains and nano-scale twins. Acta Mater 2005;53:3369–82.
[25] Rajaram G, Kumaran S, Suwas Satyam. Effect of strain rate on tensile and compression behaviour of Al–Si/graphite composite. Mater Sci Eng A 2011;528:6271–8.
[26] Dalla Torre FH, Pereloma EV, Davies CHJ. Strain rate sensitivity and apparent activation volume measurements on equal channel angular extruded Cu processed by one to twelve passes. Scripta Mater 2004;51:367–71.
[27] Wei Q, Cheng S, Ramesh KT, Ma E. Effect of nanocrystalline and ultrafine grain sizes on the strain rate sensitivity and activation volume: fcc versus bcc metals. Mater Sci Eng A 2004;381:71–9.
[28] Diologent F, Kruml T. Measurement of the effective activation volume in 45XD titanium aluminides by repeated transient tests. Mater Sci Eng A 2008;487:377–82.
[29] Viguier B, Bonneville J, Martin JL. The mechanical properties of single phase γ-$Ti_{47}Al_{51}Mn_2$ polycrystals. Acta Mater 1996;44:4403–15.
[30] Paul JDH, Appel F. Work-hardening and recovery mechanisms in gamma-based titanium aluminides. Metall Mater Trans A 2003;34:2103–11.
[31] Afrin N, Chen DL, Cao X, Jahazi M. Strain hardening behavior of a friction stir welded magnesium alloy. Scripta Mater 2007;57:1004–7.
[32] Pauly S, Das J, Duhamel C, Eckert J. Effect of titanium on microstructure and mechanical properties of $Cu_{50}Zr_{50-x}Ti_x$ ($2.5 < x < 7.5$) glass matrix composites. Metall Mater Trans A 2008;39:1868–73.